Optics Communications 423 (2018) 100–110

Contents lists available at ScienceDirect

Optics Communications

journal homepage: www.elsevier.com/locate/optcom

Modeling and image motion analysis of parallel complementary compressive sensing imaging system

Yun-Hui Li [a,b,*], Xiao-Dong Wang [a], Zhi Wang [a,c], Dan Liu [b], Ye Ding [b]

[a] Changchun Institute of Optics, Fine Mechanics and Physics, Chinese Academy of Sciences, Changchun 130033, China
[b] University of Chinese Academy of Sciences, Beijing 100049, China
[c] Changchun UP Optotech (Holding) Co., Ltd, Changchun 130033, China

ARTICLE INFO

Keywords:
Computational imaging
Compressive sensing
Parallel measurement
Image motion

ABSTRACT

Based on the theory of compressive sensing, a parallel complementary compressive sensing imaging system is proposed, and the mathematical model of block parallel processing is established. Parametric analysis shows that the quality of the restored image increases with the increase of observed compression ratio and the decrease of the number of blocks, which is in conflict with total amount of data and time-consuming of algorithm, and needs to be considered comprehensively. According to the demand of space remote sensing system applied in push-broom mode, the image motion model of the system is established. The results show that the image motion has a severe effect on the quality of restored image, and increasingly responsive with the decrease of the number of blocks. when the orbital image motion parameter is constant, improving the frame rate of the detector and increasing the pixel size can obtain a smaller image motion ratio, thereby enhancing the image quality. But the application scope of the system for push-broom imaging is somewhat limited for its significantly degrade under low image motion ratio.

1. Introduction

From the perspective of signal decomposition and approximation theory, E.J. Candes, J. Romberg, T. Tao and D.L. Donoho proposed the theory of compressed sensing(CS) in 2006 [1–3]. In the framework of this theory, if a signal is sparse in a transform domain, the sampling process will no longer be limited by the Shannon–Nyquist sampling theorem, and the original signal can be recovered from far fewer samples [4–6]. This not only reduces the requirements for hardware sampling devices, and far fewer samples can also reduce the pressure on data storage and transmission, thereby improving resource utilization.

Based on the above advantages, the compressive sensing theory has been widely concerned in the fields of medical imaging, optical radar imaging, information image processing and wireless communication. The research of computational imaging technology in the field of space remote sensing mainly focuses on high resolution imaging and multi-spectral imaging based on CS theory [7,8]. In the application of CS theory, aperture coding [9–11], digital micro-mirror device(DMD) coding [12,13], random exposure coding [14] are mostly adopted in the system to realize the random coding observation of the target signal.

The single pixel camera based on DMD is a typical application of CS theory [15–17]. It uses photodiode instead of the image sensor to complete the image sampling function, which greatly reduces the cost and the complexity of the hardware design. However, when large-scale imaging is performed, the number of coding increases, resulting in a sharp increase in observation time. Meanwhile, large-scale matrix makes the operation time of reconstruction algorithm greatly increased. The combination of the above two makes the time cost of the system larger, which sacrifices the real-time performance of the system.

Solmaz Hajmohammadi presents a parallel algorithm for handling the recursion in bispectrum phase recovery [18]. The proposed massively parallel bispectrum algorithm relies on multiple block parallelization, which achieves a speed-up of 85.94 over its recursive sequential counterpart with no loss in image quality. Aswin C. Sankaranarayanan shows two specific prototypes that achieve megapixel resolution images at video-rate by the extensions of Single Pixel Camera(SPC) [19]. A highly parallel extension of the SPC based on a focal plane array is investigated by John P. Dumas [20]. Yao Zhao et al. proposed a super resolution imaging system based on parallel compressed sensing. The proposed method first measures the transmission matrix of the scattering sheet, and parallel means that charge-coupled device camera can obtain enough measurements at once instead of changing the patterns on the DMD repeatedly [21].

* Corresponding author at: Changchun Institute of Optics, Fine Mechanics and Physics, Chinese Academy of Sciences, Changchun 130033, China.
E-mail address: liyunhui_ciomp@126.com (Y.-H. Li).

https://doi.org/10.1016/j.optcom.2018.04.018
Received 19 December 2017; Received in revised form 5 March 2018; Accepted 8 April 2018
Available online 16 May 2018
0030-4018/

B. Sun has demonstrated that a computational ghost imaging system can be readily made more robust to sources of noise, by rapid sequential projection of binary patterns and their inverse and demodulating the signals acquired from a single photodiode [22]. The sampling concept of complementary compressed sensing is proposed by Wen-Kai Yu, and applied in a telescope system with two photomultiplier tubes [23]. He also demonstrated a 3D compressive reflectivity imaging system with only a single-pixel detector and complementary intensity modulation performed by a DMD, which complies with the computer-generated random one-to-one complementary binary pattern pairs [24]. And an experiment on compressive microscopic imaging with single-pixel detector and single-arm has been performed on the basis of "positive–negative" (differential) light modulation of a digital DMD [25]. A new type of compressive spectroscopy technique employing a complementary sampling strategy is reported by Ruo-Ming Lan. In a single sequence of spectral compressive sampling, positive and negative measurements are performed, in which sensing matrices with a complementary relationship are used [26]. A.D. Rodríguez demonstrates an inverted microscope that utilizes a DMD for patterned illumination altogether with two single-pixel photo sensors for efficient light detection. The system works by sequential projection of a set of binary intensity patterns onto the sample that are codified onto a modified commercial DMD [27].

Based on the above considerations, a parallel complementary compressive sensing imaging system based on DMD is proposed in this paper. By means of two detectors sensing the light reflected in both outputs of the DMD, the measurement matrix of −1, 1 sequence is acquired without increasing the observation time, whose performance is generally better than 0, 1 sequence. Moreover, multi-block parallel coding is carried out with an array detector instead of a single pixel, which reduce the observation time and the operation time. But compared to the traditional compressive sensing system, an additional detector is added, and the subsequent driving and processing circuits are also increased, so the cost of hardware is somewhat increased.

On the basis of this system, the mathematical model of block parallel processing is established. Parameters such as number of blocks and observed compression ratio are analyzed and discussed. Then, the image motion model in the field of remote sensing imaging is established, and the performance degradation of the restored image due to image motion is quantitatively analyzed and discussed.

2. Composition of the imaging system

The schematic diagram of parallel complementary compressive sensing imaging system is shown in Fig. 1, which consists mainly of front-end lens system, DMD, matching lens system 1 and 2, and detector 1 and 2. The DMD is used as a compression encoder in the system. Each micro-mirror in DMD has 0 and 1 working states, of which 0 corresponds to the deflection of −12 degrees, and 1 corresponds to the deflection of +12 degrees. When the target scene is incident on the DMD through the front-end lens system, a part of the light is reflected by the micro-mirror in the 0 state along the direction 1, and reaches the detector 1 through the matching lens system 1. Another part of the light is reflected by the micro-mirror in the 1 state along the direction 2, and reaches the detector 2 through the matching lens system 2. The matching lens system mainly realizes the matching relationship between the micro-mirror size of DMD and the pixel size of detector.

Compared with the single-pixel imaging system, this imaging system uses an array detector instead of the photodiode as the image information receiver. At the same time, two detectors are used to collect the light reflection information of DMD under two states. Therefore, the imaging system has two significant advantages.

Firstly, with the array detector used, the target scene can be divided into blocks according to the scale of the detector pixels, that is, each encoding is performed in parallel for multiple image blocks. Since the amount of information of each sub-image block is greatly reduced with respect to the entire image, the number of parallel encoding times is greatly reduced, which thus reduces the observation time of encoding process.

Secondly, two array image detectors are used to receive the light reflection information of the two states of micro-mirror in the DMD respectively. By subtracting the data collected by each detector from each other, an observation information can be obtained, thereby the measurement matrix formed is a sequence of −1 and 1. Compared with the 0, 1 sequence, this method can obtain more image information, which resulting in a better reconstructed image with the same number of observations. Or from another point of view, this system can consume less observation time with the same reconstructed image quality.

The above description is only a qualitative analysis of the system. In the following, the mathematical model of the system will be built, and quantitative analysis and discussion of specific parameters will be carried out.

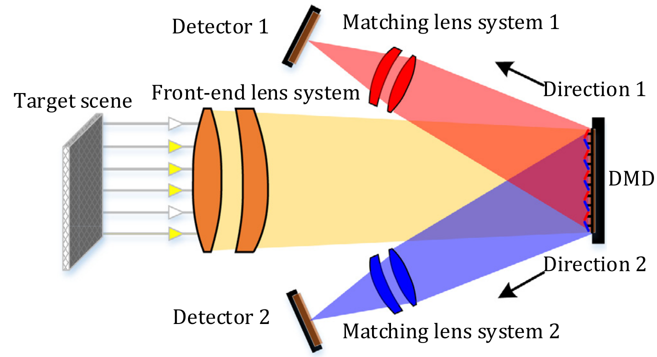

Fig. 1. The schematic diagram of parallel complementary compressive sensing imaging system.

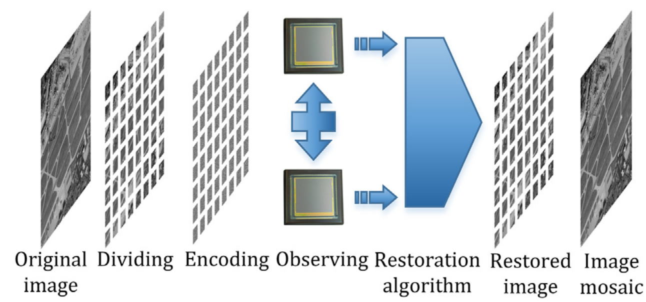

Fig. 2. The workflow of parallel complementary compressive sensing imaging system.

3. Blocking and parallel processing method

3.1. Model establishment

The workflow of the imaging system is shown in Fig. 2. Compared with the traditional compressive sensing imaging system, the target scene is divided into several blocks first, and each sub-image block is simultaneously encoded in parallel by DMD. Then two array detectors are used to receive the encoded image information, wherein each detector pixel corresponds to a sub-block. Based on the collected image information, the reconstruction of each sub-image block is completed by the image restoration algorithm, and finally the block images are spliced into the desired target scene. The number of encoding is the number of frames captured by the detector.

The algorithm theory of compressive sensing imaging system is derived from the sparse characteristics of natural images under the

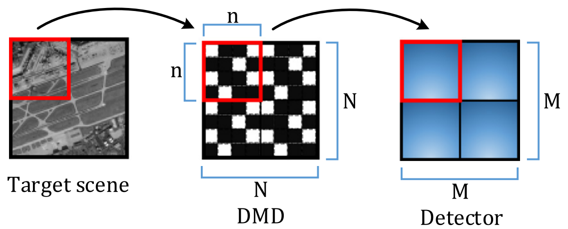

Fig. 3. The block correspondence of the components in the system.

condition of certain sparse transform bases. If the sparse representation α of the signal can be obtained by the transformation of sparse basis ψ, and the original signal x is observed by using the measurement matrix Φ, then the observation signal y can be expressed as:

$$y = \phi x = \phi\psi\alpha = T\alpha \tag{1}$$

T is the product of matrix Φ and ψ, which is called the sensing matrix.

The number of rows of the measurement matrix Φ is less than the number of columns because of the compressive sensing method. Therefore, it is an NP-hard problem, which directly calculates x from y. Under the premise that the sensing matrix T satisfies the Restrained Isometric Property(RIP), it can be solved by the l_0 norm optimization problem:

$$\alpha^* = \arg\min \|\alpha\|_0 \quad s.t. \quad y = \phi\psi\alpha \tag{2}$$

With the l_0 norm minimization problem convex-relaxed, the above problem can be transformed into L_1 norm optimization problem:

$$\alpha^* = \arg\min \|\alpha\|_1 \quad s.t. \quad y = \phi\psi\alpha \tag{3}$$

The above problem can be iteratively solved by a specific algorithm, and the Orthogonal Matching Pursuit(OMP) algorithm is used in this system. The original signal x can be obtained by multiplying the sparse basis ψ and the solved α.

As shown in Fig. 3, it is assumed that the micro-mirror array scale of DMD in the imaging system is $N \times N$, the number of pixels of the array detector is $M \times M$, that is, the number of blocks to be processed in parallel is $M \times M$, where N/M is a positive integer. If a detector pixel corresponds to a DMD sub-array of size $n \times n$, then there is $n = N/M$. The number of parallel encoding is set as m, and the ratio of parallel encoding number m to the DMD sub-array size n is defined as observed compression ratio D, that is, $D = m/n^2$.

Since each sub-block in the system is processed in the same way, the encoding and image restoration process of a sub-block to be modeled and analyzed is enough. It is assumed that the original matrix of the target scene sub-block (i, j) is $X_{i,j}$, the observation vector obtained by DMD encoding on detector 1 is $Y_{i,\ j}$, and the observation vector obtained on detector 2 is $Z_{i,j}$, where $X_{i,j}$ is n^2 rows and 1 column, $Y_{i,j}$ and $Z_{i,j}$ are

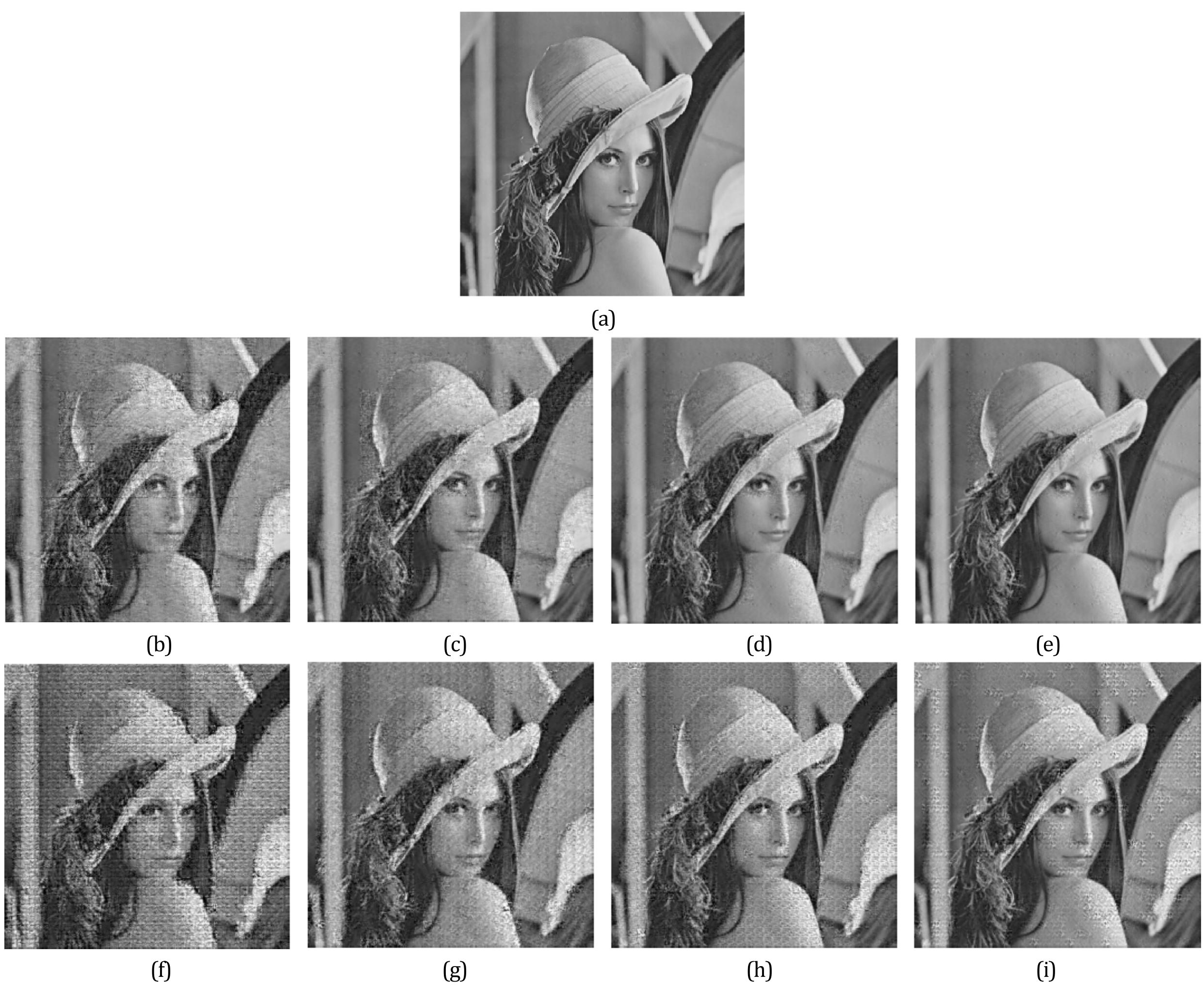

Fig. 4. The restored images of Lena. (a) Original image. (b) $M = 16$ $D = 0.6$. (c) $M = 16$ $D = 0.7$. (d) $M = 16$ $D = 0.8$. (e) $M = 16$ $D = 0.9$. (f) $M = 32$ D=0.6. (g) $M = 32$ $D = 0.7$. (h) $M = 32$ $D = 0.8$. (i) $M = 32$ $D = 0.9$.

(a)

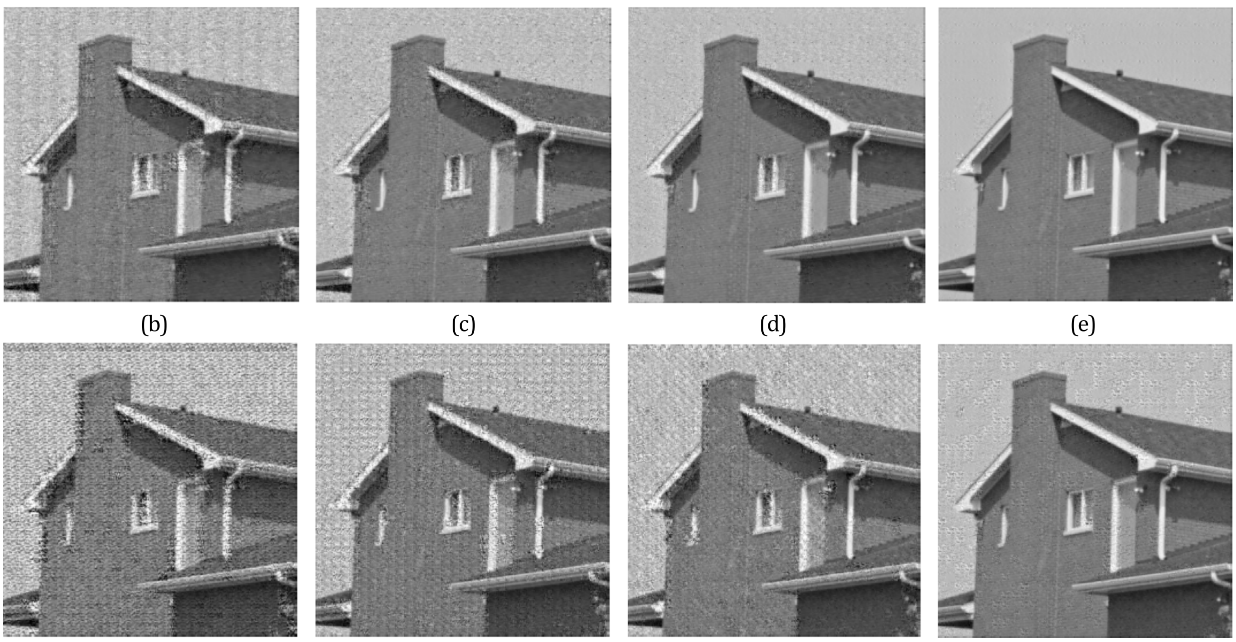

(b) (c) (d) (e)

(f) (g) (h) (i)

Fig. 5. The restored images of House. (a) Original image. (b) $M = 16$ $D = 0.6$. (c) $M = 16$ $D = 0.7$. (d) $M = 16$ $D = 0.8$. (e) $M = 16$ $D = 0.9$. (f) $M = 32$ $D = 0.6$. (g) $M = 32$ $D = 0.7$. (h) $M = 32$ $D = 0.8$. (i) $M = 32$ $D = 0.9$.

m rows and 1 column because of column processing. The measurement matrix $\Phi_{i,j}$ used on the DMD is a random Bernoulli matrix whose −1, 1 sequence is uniformly distributed, of which 1 corresponds to the state that light is reflected to detector 1, and −1 corresponds to the state that light reflected to detector 2, then the whole observation process can be expressed as:

$$Y_{i,j} - Z_{i,j} = \phi_{i,j} \cdot X_{i,j} (i, j \in (1, 2 \dots M)) \tag{4}$$

And then based on the observation results, the OMP algorithm is used to complete the sub-image block reconstruction. Discrete Cosine Transform(DCT) base is used as the sparse base matrix in this system. After getting the recovery results of each sub-image block, the final image can be easily obtained by splicing them together.

In order to compare and analyze the quality of restored image under different parameters, Peak signal to noise ratio (PSNR), Structural similarity assessment metric (SSIM) and Feature similarity index (FSIM) are selected as the evaluation standard of image quality. Where PSNR is the ratio between the maximum signal and the background noise, which is the most commonly used image quality evaluation, and larger values indicate better image quality. It simply calculates the difference of gray values between images, and the structural relationship between pixels is not considered, so the calculation results often cannot be consistent with human's subjective feelings. SSIM is used to describe the structural similarity between images, and larger values represent better image quality. According to the sensitivity of the human eyes to the structural features of an image, SSIM defines the structure information as an attribute that is independent of brightness and contrast, and reflects the structure of an object in a scene from the perspective of image composition. FSIM characterizes the feature similarity between images based on the human eye's acquisition of low-frequency feature information, which is calculated from the phase congruency (PC) and gradient magnitude (GM) information of the image. Equally larger values specific better image recovery quality [28–30].

3.2. Parametric analysis

In the imaging process of the system, the ultimate goal is to optimize the quality of the restored image with the highest *PSNR* value, which is closely related to the observed compression ratio D and the number of blocks M. The observed compression ratio D affects the total amount of data S that the system needs to collect. The total amount of data S required for the entire target scene acquisition in the system can be expressed as:

$$S = n^2 \times D \times M^2 = D \cdot N^2 \tag{5}$$

That is, the total amount of data S is proportional to the observed compression ratio D, so the larger the compression ratio D is, the greater the data storage and transmission pressure of the system is. While the number of blocks M corresponds to the number of pixels required by the detector, and it also affects the consumption time of recovery algorithm.

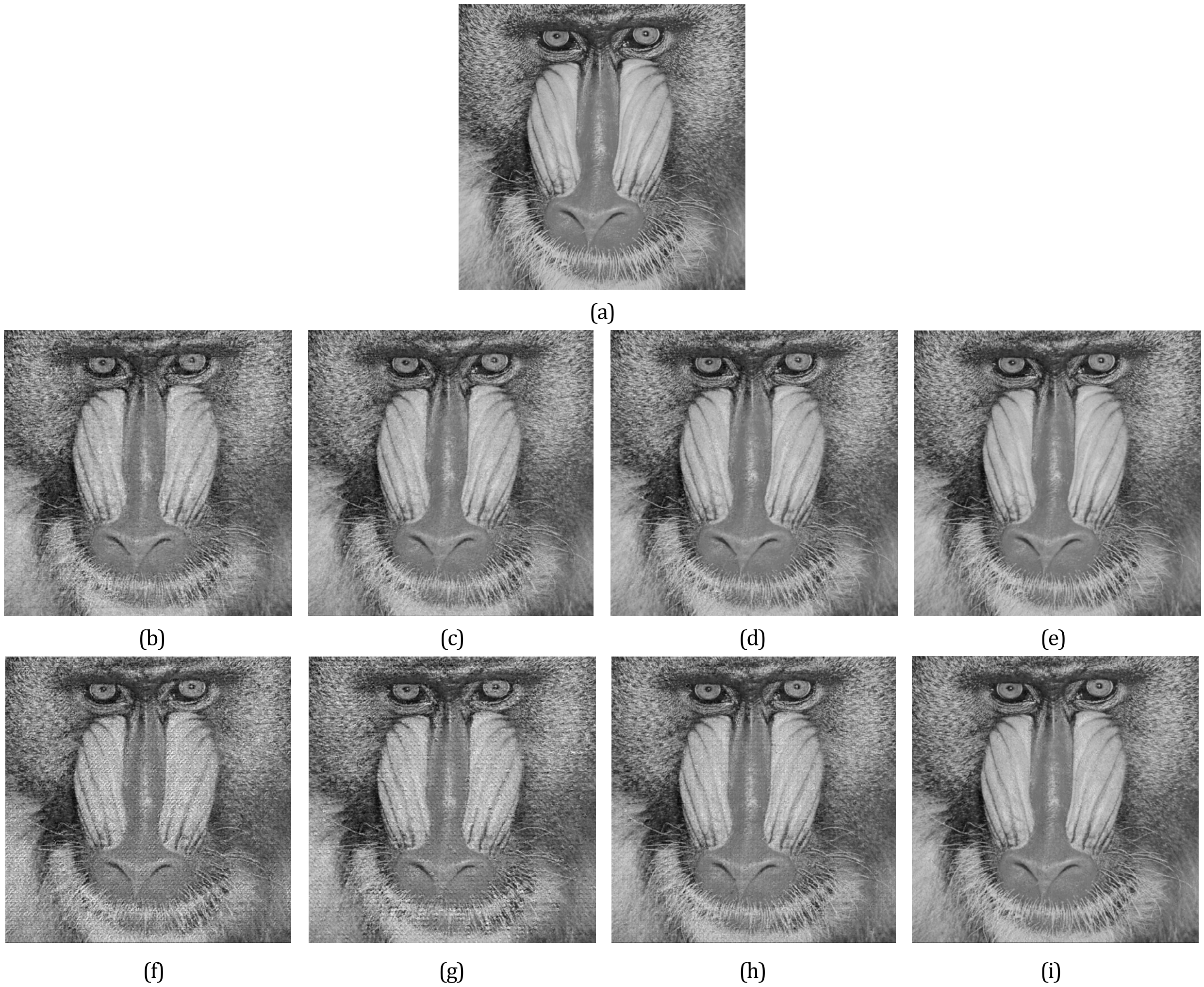

Fig. 6. The restored images of Mandrill. (a) Original image. (b) $M = 32$ $D = 0.6$. (c) $M = 32$ $D = 0.7$. (d) $M = 32$ $D = 0.8$. (e) $M = 32$ $D = 0.9$. (f) $M = 64$ $D = 0.6$. (g) $M = 64$ $D = 0.7$. (h) $M = 64$ $D = 0.8$. (i) $M = 64$ $D = 0.9$.

In order to verify the universal applicability of the above imaging system, multiple images of different types and resolutions were taken for simulation verification. The specific simulation results are shown in Fig. 4 to Fig. 9. Among them, Figs. 4 and 5 are natural images with the resolution of 256 × 256, Figs. 6 and 7 are natural images with the resolution of 512 × 512, and the remote sensing images with the resolution of 2048 × 2048 are shown in Figs. 8 and 9.

For quantitative analysis, the PSNR, SSIM and FSIM values of the above images were calculated respectively, as shown in Table 1. According to the data of the three indexes in the table, the changing trend of the three are always consistent under the conditions of different parameters M and D. Therefore, PSNR will be taken as the representation of the image quality evaluation standard in the following. It can be seen from the table that the quality of the image restoration with different types and resolutions is consistent with the change of the parameters M and D. That is to say, the image quality increases with the increase of D in the same number of blocks M. For the same parameter D, smaller values of M acquire higher quality images.

After verifying the effectiveness of the system, detailed analysis will be performed on the image of Remote1 below. According to the data obtained from the restored image, the *PSNR* of the restored image are calculated under a larger parameter range, and the drawing curves are shown in Fig. 10. The dotted lines in the figure are the calculation results of using measurement matrix with 0, 1 sequence.

It can be seen from the above results, firstly, the quality of the image restoration using measurement matrix with −1, 1 sequence is generally better than that of 0, 1 sequence, and the gap becomes more obvious with the increase of *PSNR* value. So it is necessary to use two detectors for complementary observation.

Secondly, on the premise of the same number of blocks M, the value of *PSNR* increases with the increase of observed compression ratio D, which is not difficult to understand, because the larger the observed compression ratio is, the larger the amount of information obtained by the system is, and the quality of restored image will naturally improve. However, the observed compression ratio is directly proportional to the total amount of data. Therefore, using too high compression ratio to enhance the image quality will aggravate the burden of image storage and transmission.

Thirdly, with the increase of the number of blocks M, the *PSNR* of the restored image gradually decreases. In order to explain the reason, we introduce the definition of sparsity δ_k, which is the ratio of the number k of non-zero values of the original image after sparse basis transform to the original signal length x_l, and it can be expressed as:

$$\delta_k = \frac{k}{x_l} \tag{6}$$

Since the remote sensing image is not ideal sparse feature after sparse basis transform, there exist lots of non-zero values which are close to 0. Therefore, under the condition of 256 grayscale levels, the threshold is set to 10, which higher than that is seen as a non-zero value and counted into the k. With different number of sub-blocks, the remote sensing image is transformed by DCT basis, and the sparsity δk of each sub-block obtained is shown in Fig. 11.

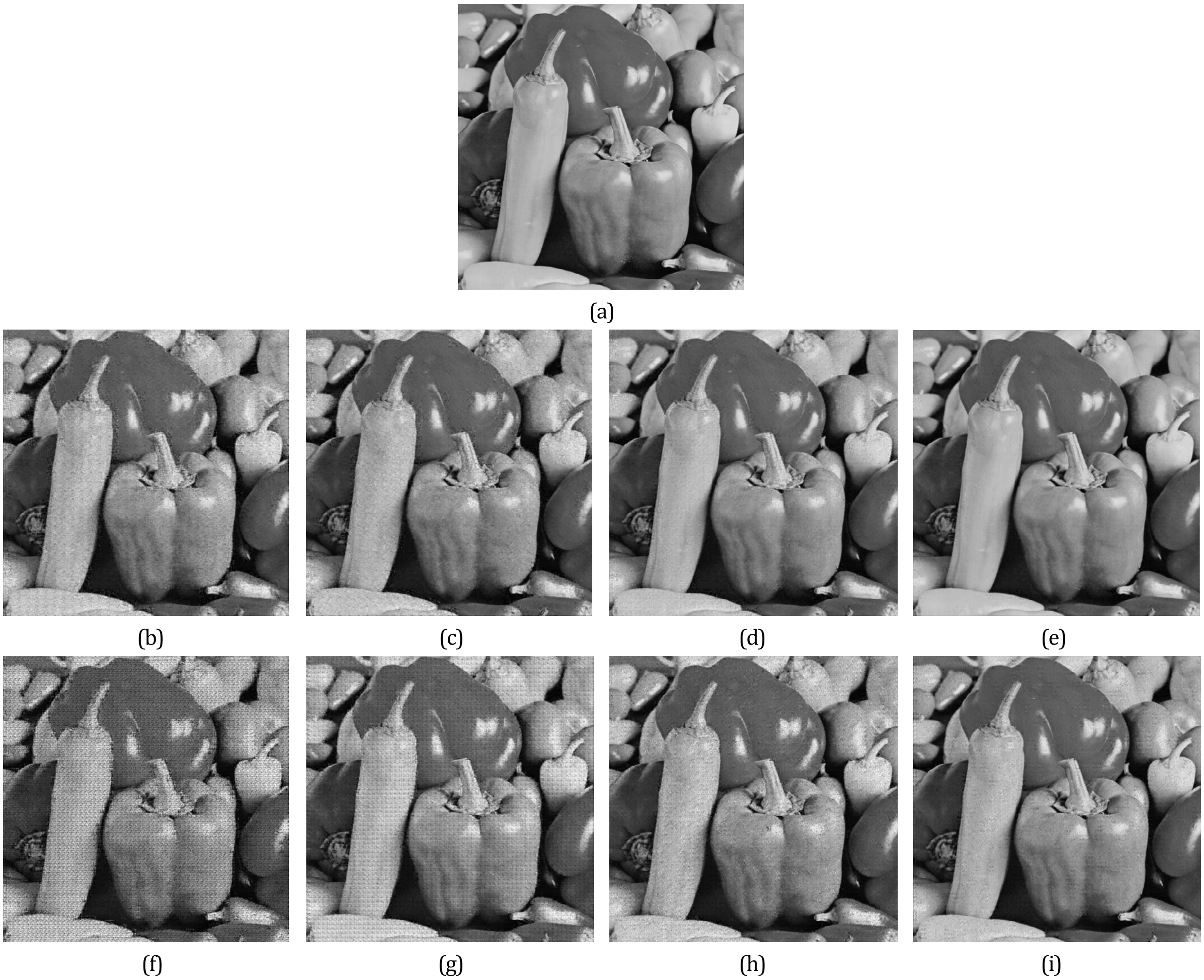

Fig. 7. The restored images of Peppers. (a) Original image. (b) $M = 32$ $D = 0.6$. (c) $M = 32$ $D = 0.7$. (d) $M = 32$ $D = 0.8$. (e) $M = 32$ $D = 0.9$. (f) $M = 64$ $D = 0.6$. (g) $M = 64$ $D = 0.7$. (h) $M = 64$ $D = 0.8$. (i) $M = 64$ $D = 0.9$.

Table 1
The quantitative results of the above images with the indexes of PSNR, SSIM and FSIM.

Images	Resolution	Measures	$M = 16$				$M = 32$			
			$D = 0.6$	$D = 0.7$	$D = 0.8$	$D = 0.9$	$D = 0.6$	$D = 0.7$	$D = 0.8$	$D = 0.9$
		PSNR	23.97 dB	26.37 dB	29.86 dB	32.69 dB	20.37 dB	23.48 dB	24.39 dB	26.09 dB
Lena	256 × 256	SSIM	0.9431	0.9670	0.9851	0.9922	0.8769	0.9367	0.9490	0.9655
		FSIM	0.8049	0.8711	0.9342	0.9653	0.6859	0.7800	0.7998	0.84210
		PSNR	26.07 dB	29.06 dB	32.19 dB	37.23 dB	20.58 dB	23.52 dB	25.01 dB	29.38 dB
House	256 × 256	SSIM	0.9626	0.9809	0.9907	0.9971	0.8757	0.9346	0.9527	0.9824
		FSIM	0.8199	0.8831	0.9320	0.9748	0.6770	0.7667	0.7973	0.9011
Images	Resolution	Measures	$M = 32$				$M = 64$			
			$D = 0.6$	$D = 0.7$	$D = 0.8$	$D = 0.9$	$D = 0.6$	$D = 0.7$	$D = 0.8$	$D = 0.9$
		PSNR	21.18 dB	23.43 dB	25.23 dB	28.00 dB	19.65 dB	20.47 dB	23.33 dB	27.07 dB
Mandrill	512 × 512	SSIM	0.8414	0.8956	0.9291	0.9594	0.8171	0.8415	0.9076	0.9561
		FSIM	0.8815	0.9264	0.9485	0.9761	0.8646	0.8727	0.9280	0.9696
		PSNR	26.19 dB	27.93 dB	31.68 dB	37.21 dB	20.20 dB	24.03 dB	26.37 dB	29.49 dB
Peppers	512 × 512	SSIM	0.9672	0.9788	0.9906	0.9977	0.8791	0.9470	0.9708	0.9844
		FSIM	0.8992	0.9261	0.9688	0.9944	0.8129	0.8522	0.9071	0.9543
Images	Resolution	Measures	$M = 128$				$M = 256$			
			$D = 0.6$	$D = 0.7$	$D = 0.8$	$D = 0.9$	$D = 0.6$	$D = 0.7$	$D = 0.8$	$D = 0.9$
		PSNR	24.01 dB	28.83 dB	35.81 dB	37.36 dB	18.64 dB	22.49 dB	27.02 dB	32.53 dB
Remote1	2048 × 2048	SSIM	0.9371	0.9597	0.9907	0.9939	0.8570	0.9108	0.9539	0.9850
		FSIM	0.9855	0.9971	0.9997	0.9999	0.9542	0.9776	0.9952	0.9994
		PSNR	25.56 dB	29.75 dB	36.17 dB	37.96 dB	19.72 dB	23.38 dB	28.86 dB	33.83 dB
Remote2	2048×2048	SSIM	0.9365	0.9680	0.9894	0.9966	0.8853	0.9118	0.9609	0.9866
		FSIM	0.9883	0.9983	0.9998	0.9999	0.9689	0.9831	0.9965	0.9996

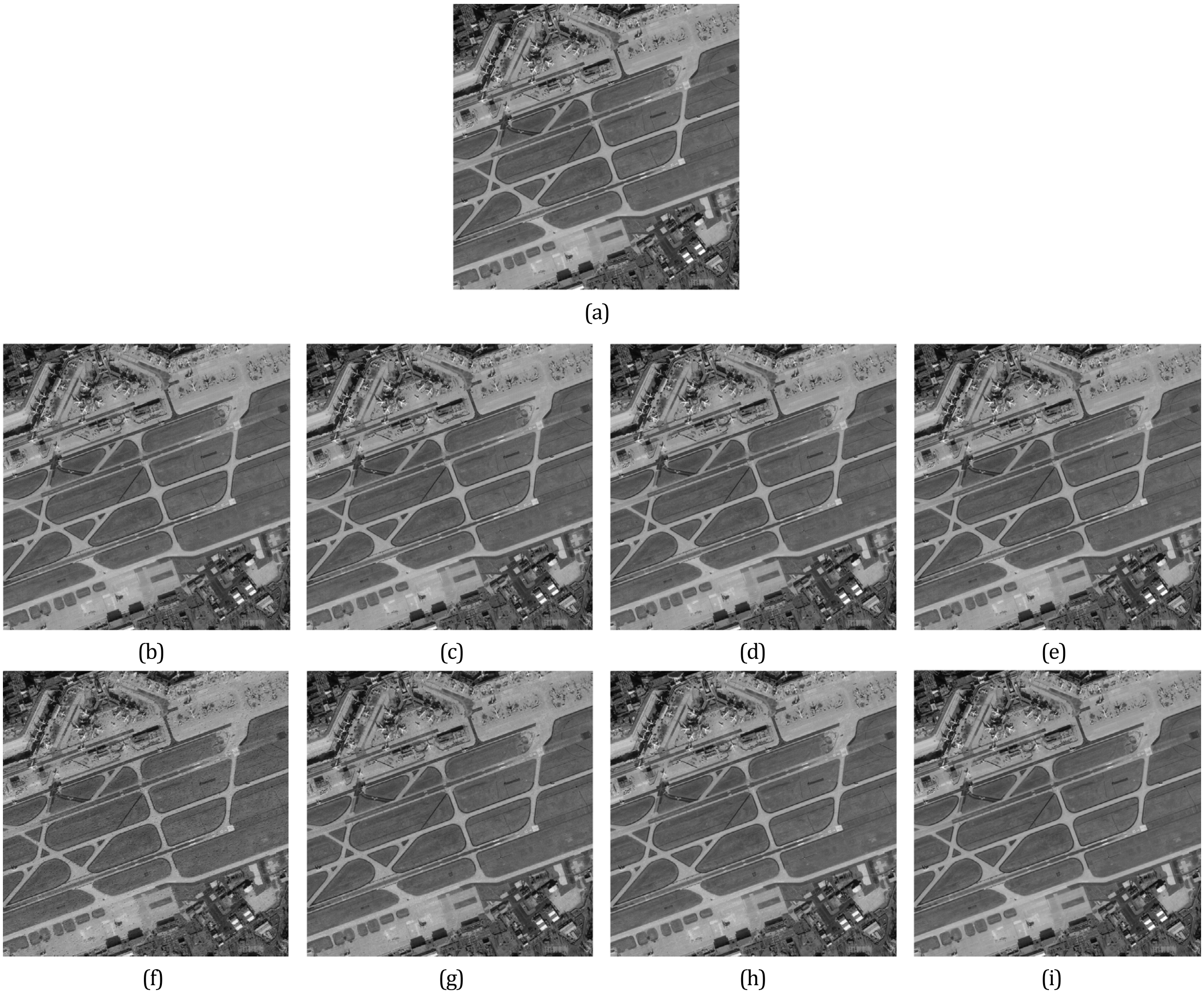

Fig. 8. The restored images of Remote1. (a) Original image. (b) $M = 128$ $D = 0.6$. (c) $M = 128$ $D = 0.7$. (d) $M = 128$ $D = 0.8$. (e) $M = 128$ $D = 0.9$. (f) $M = 256$ $D = 0.6$. (g) $M = 256$ $D = 0.7$. (h) $M = 256$ $D = 0.8$. (i) $M = 256$ $D = 0.9$.

It can be seen from Fig. 11 that, with the number of sub-blocks increasing, the sparsity δ_k in each sub-block gradually increases and the sparseness deteriorates. This can be explained by the fact that the properties of natural image in each sub-block are degraded as the sub-blocks become more and more refined, which leads to the sparseness degradation. Therefore, *PSNR* will decrease with the increase of *M*, when the same observed compression ratio *D* is used. In other words, on the premise of the same total amount of data, the smaller the number of blocks *M*, the higher the value of *PSNR*. However, the decrease of *M* results in an increase in the size of the measurement matrix, which leads to a time-consuming increase of the restoration algorithm, as shown in Fig. 12, which are performed using MATLAB software on a PC with a dual core Intel i5 2.5 GHz CPU. Furthermore, the real-time performance of remote sensing image acquisition is degraded, so it needs to be considered comprehensively in practical application.

4. Impact of image motion

4.1. Model establishment

The imaging system described in this paper requires multiple coding of the same target scene, which is theoretically suitable for the gaze imaging system. While the space remote sensing system usually works in the push-sweep mode because of the characteristics of its orbit. If this system is used in the push-sweep mode, there will be a decline in the quality of restored image due to the image motion during the multiple coding of a target scene. For quantitative analysis, the image motion model of the system is established below.

The coding rate of the system depends on the refresh rate of DMD and the frame rate of array detector, and takes the lower value of the two. Constrained by the limitation of DMD and detector, it is assumed that the time required for single observation is *t*, and the moving speed of target scene on the focal plane is *v*. Then the image motion of two adjacent observations is $v \times \Delta t$. Fig. 13 is the schematic diagram of image motion in the encoding process.

The pixel size of the detector is set to *a*, and one detector pixel corresponding to the sub-array size of DMD is $n \times n$, then the image motion ratio *p* within two adjacent observations is as follows:

$$p = \frac{v \times \Delta t}{a/n} \tag{7}$$

If the image motion is zero at the first observation, then the image motion ratio P_k of the kth observation can be expressed as:

$$P_k = (k-1) \cdot p(k \in (1, 2 \ldots m)) \tag{8}$$

The original data of the sub-block (i, j) that is to be observed is matrix *X*, which can be expressed as:

$$X = \begin{bmatrix} x_{1,1} & \cdots & x_{1,n} \\ \vdots & \ddots & \vdots \\ x_{n,1} & \cdots & x_{n,n} \end{bmatrix} \tag{9}$$

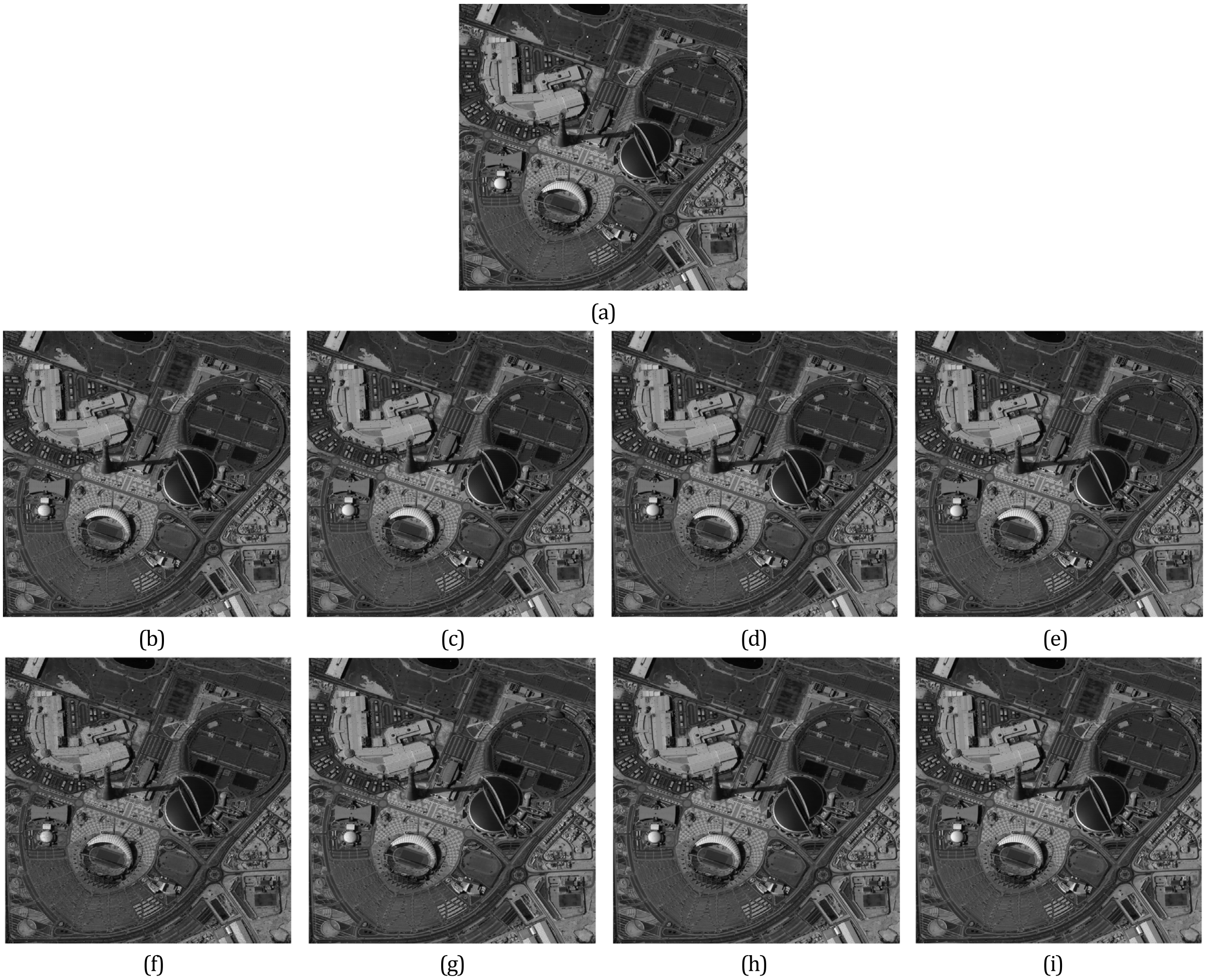

Fig. 9. The restored images of Remote2. (a) Original image. (b) $M = 128$ $D = 0.6$. (c) $M = 128$ $D = 0.7$. (d) $M = 128$ $D = 0.8$. (e) $M = 128$ $D = 0.9$. (f) $M = 256$ $D = 0.6$. (g) $M = 256$ $D = 0.7$. (h) $M = 256$ $D = 0.8$. (i) $M = 256$ $D = 0.9$.

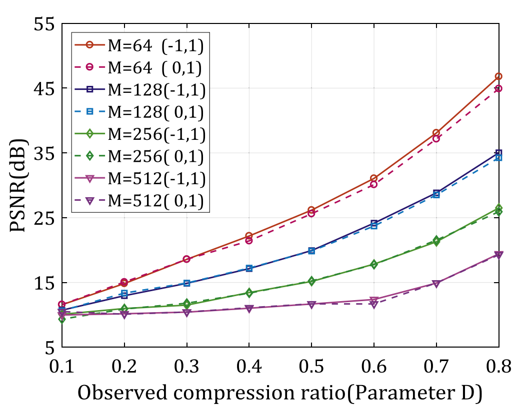

Fig. 10. The relationship between PSNR and observed compression ratio in different number of blocks.

The result of m observations is the matrix Y of m rows and 1 column:

$$Y = \begin{bmatrix} y_{1,1} & \cdots & y_{m,1} \end{bmatrix}^T \tag{10}$$

There is no image motion for the first observation, so the target scene matrix $X^1 = X$. Then the matrix X^1 is arranged in a column, and the matrix CX^1 is formed.

$$CX^1 = \begin{bmatrix} x^1{}_{1,1} & \cdots & x^1{}_{1,n} & x^1{}_{2,1} & \cdots & x^1{}_{2,n} & x^1{}_{n,1} & \cdots & x^1{}_{n,n} \end{bmatrix}^T \tag{11}$$

The first observation result $b_{1,1}$ is obtained from the following equation, where $\Phi_{1,:}$ is the first row of the measurement matrix.

$$b_{1,1} = \phi_{1,:} \cdot CX^1 \tag{12}$$

When this sub-block is observed for the kth time, the target scene X^k becomes:

$$X^k = \begin{bmatrix} x^k{}_{1,1} & \cdots & x^k{}_{1,n} \\ \vdots & \ddots & \vdots \\ x^k{}_{n,1} & \cdots & x^k{}_{n,n} \end{bmatrix} \tag{13}$$

Each element in the matrix above is calculated as follows:

$$x_{i,j}{}^k = (1 - (P_k - \lfloor P_k \rfloor)) \cdot x_{i+\lfloor P_k \rfloor, j} + (P_k - \lfloor P_k \rfloor) \cdot x_{i+\lceil P_k \rceil, j} \tag{14}$$

Where $\lfloor\ \rfloor$ means rounding down, $\lceil\ \rceil$ means rounding up, and $i, j \in [1, n]$. Due to the existence of image motion, the data sampling process is beyond the data range of the original image $n \times n$. Therefore, the image data outside the target image area needs to be introduced. Assuming that the image motion process is along the line direction of the image, more image data in the image motion direction is required. The specific application data range is $x_{i,j}$ ($i \in [1, n + \lceil P_k \rceil]$, $j \in [1, n]$. The

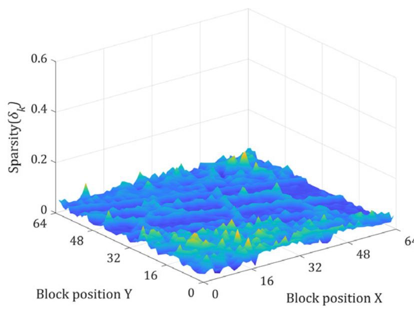

(a) $M = 64$.

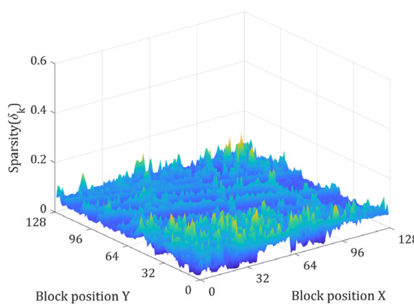

(b) $M = 128$.

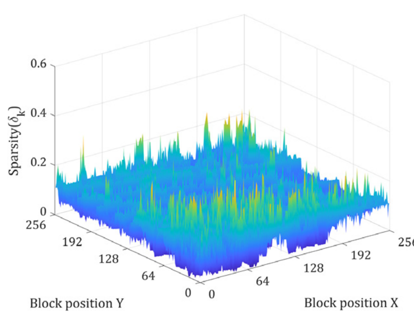

(c) $M = 256$.

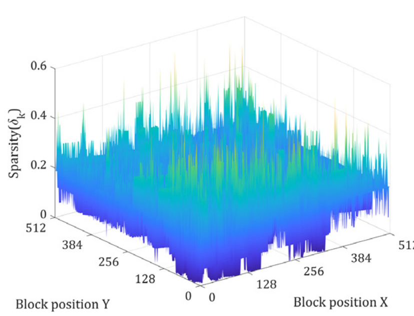

(d) $M = 512$.

Fig. 11. The sparsity of the image with different number of blocks.

subsequent simulation process should take into account the adequacy of the image data. Based on Eq. (14), the matrix X^k is arranged in a column, and the matrix CX^k is formed.

$$CX^k = \left[x^k{}_{1,1} \quad \cdots \quad x^k{}_{1,n} \quad x^k{}_{2,1} \quad \cdots \quad x^k{}_{2,n} \quad x^k{}_{n,1} \quad \cdots \quad x^k{}_{n,n}\right]^T \tag{15}$$

The kth observation result $b_{k,1}$ is obtained from the following equation, where $\Phi_{k,:}$ is the kth row of the measurement matrix.

$$b_{k,1} = \phi_{k,:} \cdot CX^k \tag{16}$$

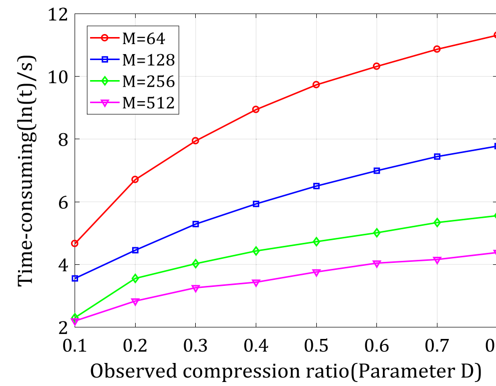

Fig. 12. The relationship between time-consuming and observed compression ratio in different number of blocks.

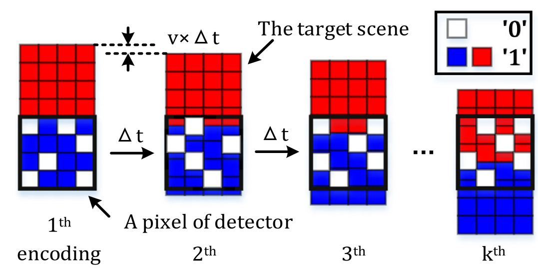

Fig. 13. The schematic diagram of image motion in the encoding process.

4.2. Parametric analysis

In the above model, when the system hardware parameters are determined, the image motion ratio p is proportional to the target push-broom speed, which indicates the application environment of the system. According to Eq. (8), the total image motion P of the observation process is affected by the observation times m. While based on $m = D(M/N)^2$, the observation times m is affected by the number of blocks M and the observed compression ratio D. Therefore, the *PSNR* of the restored image will be analyzed below with respect to the image motion ratio p, the number of blocks M, and the observed compression ratio D parameters.

For the convenience of detail observation and the adequacy of the image data, the typical local area of the above remote sensing image Remote1 is taken as the analysis object with a resolution of 256×256, which guarantees that the sampling data of the entire image motion process will not exceed the overall image data of 2048 × 2048 resolution. Fig. 14 shows the restored images obtained with different number of blocks M and image motion ratio p. According to the data obtained from the restored image, the PSNR values of the reconstructed image are calculated under different parameters, and the drawing curves are shown in Figs. 15 and 16, wherein Fig. 15 shows the case of $M = 128$, and Fig. 16 shows the case of $M = 256$.

First of all, by comparing the two figures, it can be seen that the smaller the number of blocks M is, the more sensitive the *PSNR* is to parameter p, and the sensitivity of *PSNR* to p is about 1‰ when $M = 128$, while the sensitivity of *PSNR* to p is about 5‰ when $M = 256$.

Secondly, the overall trend shows that the *PSNR* of restored image gradually decreases with the increase of the image motion ratio p. This indicates that the image motion does have a negative impact on the restoration of the image.

Thirdly, when the parameter p is fixed to several values, the *PSNR* increases first and then decreases with the increase of the observed compression ratio D, and there exists a maximum point. This can be explained as follows. At the stage of low observed compression ratio,

(a) $M = 128$ $p = 0$.

(b) $M = 128$ $p = 0.001$.

(c) $M = 128$ $p = 0.003$.

(d) $M = 128$ $p = 0.005$.

(e) $M = 256$ $p = 0$.

(f) $M = 256$ $p = 0.01$.

(g) $M = 256$ $p = 0.02$.

(h) $M = 256$ $p = 0.03$.

Fig. 14. The restored images with different number of blocks and image motion ratio, where $D = 0.8$.

the amount of observation data increases with the increase of D, which is beneficial to image restoration, thus increasing the *PSNR*. At the stage of high observed compression ratio, the total image motion P of the observation process also increases linearly with the increase of D, and the image quality degradation caused by image motion becomes prominent, resulting in a decrease in *PSNR*.

Fig. 17 shows a trend diagram for the change of *PSNR* with parameter p and D. Under the condition of high compression ratio and low image motion ratio, either the decrease of observed compression ratio D or the increase of image motion ratio p will lead to a sharp deterioration of

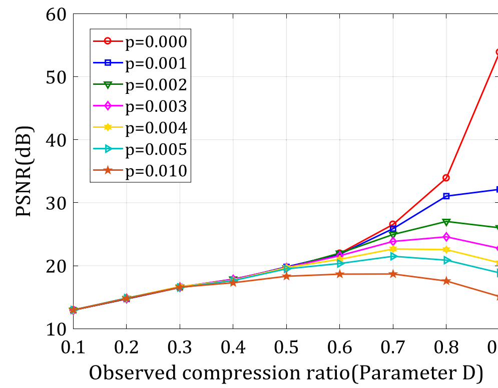

Fig. 15. The relationship between PSNR and observed compression ratio in different image motion ratio, where $M = 128$.

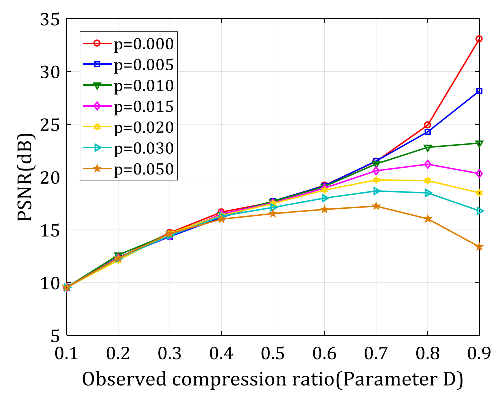

Fig. 16. The relationship between PSNR and observed compression ratio in different image motion ratio, where $M = 256$.

restored image quality. In particular, the imaging quality of the system is more sensitive to the image motion ratio p.

Therefore, in order to achieve high quality restored image, it is crucial to reduce p while using high compression ratio D. However, the image motion ratio p is closely related to the system application environment and the system hardware parameters. From Eq. (7), it can be seen that when the orbital image motion parameter is constant, improving the frame rate of the detector for reducing the single observation time and increasing the pixel size can obtain a smaller image motion ratio p, thereby enhancing the image quality. Meanwhile, it must be pointed out that the image quality has been significantly degraded under the low image motion ratio p, so the application scope of the system for push-scan imaging is somewhat limited.

5. Conclusion

In this paper, a parallel complementary compressive sensing imaging system based on DMD is proposed, and the mathematical model of block parallel processing is established on the basis of this system. Parametric analysis shows that the PSNR increases with the increase of observed compression ratio and the reduction of the number of blocks. However, the observed compression ratio has a positive correlation with the total amount of data, and the number of blocks is negatively correlated with the algorithm time-consuming. Therefore, the relationship between the image quality and total amount of data, time-consuming of algorithm is contradictory, which needs to be comprehensively considered.

According to the demand of space remote sensing imaging in push-broom mode, the image motion model of the system is established. The results show that the image motion has a severe effect on the quality

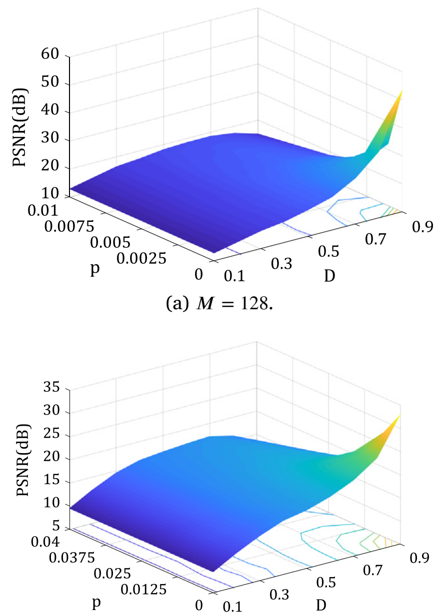

(a) $M = 128$.

(b) $M = 256$.

Fig. 17. The trend for the change of PSNR with parameter p and D.

of restored image, and increasingly responsive with the decrease of the number of blocks. In order to achieve high quality restored image, it is crucial to reduce image motion ratio while using high compression ratio. when the orbital image motion parameter is constant, improving the frame rate of the detector for reducing the single observation time and increasing the pixel size can obtain a smaller image motion ratio, thereby enhancing the image quality. Meanwhile, it must be pointed out that the image quality has been significantly degraded under the low image motion ratio, so the application scope of the system for push-scan imaging is somewhat limited.

Acknowledgment

This work is supported by Technology Innovation and Achievement Transformation Project of Jilin Province of China [Grant No. 20150312039ZG].

References

[1] D.L. Donoho, Compressed sensing, IEEE Trans. Inform. Theory 52 (2006) 1289–1306.
[2] E.J. Candès, Compressive sampling, Marta Sanz Solé 17 (2006) 1433–1452.
[3] E.J. Candes, J. Romberg, T. Tao, Robust uncertainty principles: exact signal reconstruction from highly incomplete frequency information, IEEE Trans. Inform. Theory 52 (2006) 489–509.
[4] Emmanuel J. Candes, Michael B. Wakin, An introduction to compressive sampling, IEEE Signal Process. Mag. 25 (2008) 21–30.
[5] Richard G. Baraniuk, Compressive sensing, IEEE Signal Process. Mag. 24 (2007) 118–121.
[6] Joel A. Tropp, Jason N. Laska, Marco F. Duarte, et al., Beyond nyquist: Efficient sampling of sparse bandlimited signals, IEEE Trans. Inform. Theory 56 (2010) 520–544.
[7] James E. Fowler, Compressive pushbroom and whiskbroom sensing for hyperspectral remote-sensing imaging, in: IEEE International Conference on Image Processing, ICIP, 2014, pp. 684–688.
[8] S.J. Sreeja, M. Wilscy, Single image super-resolution based on compressive sensing and TV minimization sparse recovery for remote sensing images, in: IEEE Recent Advances in Intelligent Computational Systems, RAICS, 2013, pp. 215–220.
[9] Laura Galvis, Henry Arguello, Gonzalo R. Arce, Coded aperture design in mismatched compressive spectral imaging, Appl. Opt. 54 (2015) 9875–9882.
[10] Laura Galvis, Daniel Lau, Xu Ma, et al., Coded aperture design in compressive spectral imaging based on side information, Appl. Opt. 56 (2017) 6332–6340.
[11] Laura Galvis, Henry Arguello, Gonzalo R. Arce, Synthetic coded apertures in compressive spectral imaging, in: IEEE International Conference on Acoustic, Speech and Signal Processing, 2014, pp. 3181–3185.
[12] Zhongqiu Sun, Bo Chen, Chengqi Cheng, A DMD-based hyperspectral imaging system using compressive sensing method, in: Proc. of SPIE 9263.
[13] Bing Ouyang, Weilin Hou, Cuiling Gong, et al., Experimental study of a DMD based compressive line sensing imaging system in the turbulence environment, in: Proc. of SPIE 9761.
[14] Guangming Shi, Dahua Gao, Xiaoxia Song, et al., High-resolution imaging via moving random exposure and its simulation, IEEE Trans. Image Process. 20 (2011) 276–282.
[15] Liang Gao, Jinyang Liang, Chiye Li, et al., Single-shot compressed ultrafast photography at one hundred billion frames per second, Nature 516 (2014) 74–77.
[16] Gongxin Li, Wenxue Wang, Yuechao Wang, et al., Single-pixel camera with one graphene photodetector, Opt. Express 24 (2016) 400–408.
[17] Jaewook Shin, Bryan T. Bosworth, Mark A. Foster, Single-pixel imaging using compressed sensing and wavelength-dependent scattering, Opt. Lett. 41 (2016) 886–889.
[18] Solmaz Hajmohammadi, Saeid Nooshabadi, Jeremy P. Bos, Massive parallel processing of image reconstruction from bispectrum through turbulence, Appl. Opt. 54 (2015) 9370–9378.
[19] Aswin C. Sankaranarayanan, Ashok Veeraraghavan, Parallel compressive imaging, in: Imaging and Applied Optics 2015, OSA Technical Digest(online) (Optical Society of America, 2015), paper CTh3E.4.
[20] John P. Dumas, Muhammad A. Lodhi, Waheed U. Bajwa, Mark C. Pierce, Computational imaging with a highly parallel image-plane-coded architecture: challenges and solutions, Opt. Express 24 (2016) 6145–6155.
[21] Yao Zhao, Qian Chen, Shenghang Zhou, et al., Super-resolution imaging through scattering medium based on parallel compressed sensing, IEEE Photon. J. 9 (2017) 7803012.
[22] B. Sun, M.P. Edgar, R. Bowman, et al., Differential Computational Ghost Imaging, in Imaging and Applied Optics 2013, OSA Technical Digest(Online), Optical Society of America, 2013 paper CTu1C.4.
[23] Wen-Kai Yu, Xue-Feng Liu, Xu-Ri Yao, et al., Complementary compressive imaging for the telescopic system, Sci. Rep. 4 (2014) 5834.
[24] Wen-Kai Yu, Xu-Ri Yao, Xue-Feng Liu, et al., Three-dimensional single-pixel compressive reflectivity imaging based on complementary modulation, Appl. Opt. 54 (2015) 363–367.
[25] Wen-Kai Yu, Xu-Ri Yao, Xue-Feng Liu, et al., Compressive microscopic imaging with "positive–negative" light modulation, Opt. Commun. 371 (2016) 105–111.
[26] Ruo-Ming Lan, Xue-Feng Liu, Xu-Ri Yao, et al., Single-pixel complementary compressive sampling spectrometer, Opt. Commun. 366 (2016) 349–353.
[27] A.D. Rodríguez, P. Clemente, E. Tajahuerce, et al., Dual-mode optical microscope based on single-pixel imaging, Opt. Lasers Eng. 82 (2016) 87–94.
[28] S. Vishnukumar, M. Wilscy, Single image super-resolution based on compressive sensing and improved TV minimization sparse recovery, Opt. Commun. 404 (2017) 80–93.
[29] Z. Wang, A.C. Bovik, H.R. Sheikh, E.P. Simoncelli, Image quality assessment: from error visibility to structural similarity, IEEE Trans. Image Process. 13 (2004) 600–612.
[30] Lin Zhang, Lei Zhang, X. Mou, D. Zhang, FSIM: A Feature similarity index for image quality assessment, IEEE Trans. Image Process 20 (2011) 2378–2386.